

## Photocatalytic Performance of Ta<sub>2</sub>O<sub>5</sub>/BiVO<sub>4</sub> Heterojunction for Hydrogen Production and Methylene Blue Photodegradation

Henrique B. Gonçalves,<sup>1b, a, b</sup> Denilson V. Freitas,<sup>1b, a</sup> Emanuely J. Souza,<sup>1b, a</sup>  
Mauricio A. Melo,<sup>1b, c</sup> Johan R. Gonzalez-Moya,<sup>1b, d</sup> Eduardo Padrón-Hernández,<sup>1b, b</sup>  
Sherdil Khan<sup>1b, e</sup> and Giovanna Machado<sup>1b, \*, a, b</sup>

<sup>a</sup>Laboratório de Pesquisa em Nanotecnologia,  
Centro de Tecnologias Estratégicas do Nordeste (CETENE), 50740-540 Recife-PE, Brazil

<sup>b</sup>Programa de Pós-Graduação em Ciência de Materiais,  
Universidade Federal de Pernambuco, 50670-901 Recife-PE, Brazil

<sup>c</sup>Instituto de Química, Universidade Federal Fluminense, Outeiro de São João Batista,  
Campus do Valonguinho, 24020-141 Niterói-RJ, Brazil

<sup>d</sup>Department of Chemistry and Biochemistry, Florida International University,  
11200 SW 8th Street, Miami, Florida 33199, United States

<sup>e</sup>Laboratório de Filmes Finos e Fabricação de Nanoestruturas (L3FNano), Instituto de Física,  
Universidade Federal do Rio Grande do Sul (UFRGS), 90650-001 Porto Alegre-RS, Brazil

Forming semiconductor heterojunction is promising for improved photocatalytic performance due to synergistic combination of the best properties of each material. The present study reports a simple hydrothermal strategy to form n-n heterojunction of Ta<sub>2</sub>O<sub>5</sub> nanotubes and BiVO<sub>4</sub> microstructures. The Ta<sub>2</sub>O<sub>5</sub>/BiVO<sub>4</sub> heterojunctions were characterized by Raman spectroscopy, UV-Vis diffuse reflectance spectroscopy (DRS), X-ray diffraction (XRD), scanning electron microscopy (SEM) and their photocatalytic activity was evaluated by hydrogen production and photodegradation of methylene blue (MB) dye in aqueous medium under AM 1.5 G (100 mW cm<sup>-2</sup>) condition. The heterojunctions have optical absorption in the visible region (200-500 nm) with crystal structures defined as monoclinic for BiVO<sub>4</sub> and orthogonal for Ta<sub>2</sub>O<sub>5</sub>. For MB photodegradation, the Ta<sub>2</sub>O<sub>5</sub>/BiVO<sub>4</sub> obtained via hydrothermal route showed a photodegradation of 72.3%, compared to 28.3% presented by the sample produced through the mechanical mixture, with the maintenance of 86.4% of its photocatalytic performance after 3 cycles of photodegradation. For H<sub>2</sub> production, hydrothermally prepared Ta<sub>2</sub>O<sub>5</sub>/BiVO<sub>4</sub> generated 10.2 μmol g<sup>-1</sup> of H<sub>2</sub> in 3 h; while Ta<sub>2</sub>O<sub>5</sub> nanotubes and mechanical Ta<sub>2</sub>O<sub>5</sub>/BiVO<sub>4</sub> mixture shows 6.82 and 2.80 μmol g<sup>-1</sup>, respectively. The results suggest that Ta<sub>2</sub>O<sub>5</sub>/BiVO<sub>4</sub> is a promising material for applications in photocatalysis, promoting sustainable energy production through hydrogen and for the treatment of effluents containing cationic dyes.

**Keywords:** photocatalysis, hydrogen, n-n heterojunction, tantalum dioxide, photodegradation

### Introduction

Due to the current serious problems of environmental management and non-renewable energy generation, efficient, clean and low-cost systems for environmental remediation and green energy generation are necessary to guarantee better conditions for the next generations.<sup>1</sup> For

power generation, the hydrogen (H<sub>2</sub>) is an eco-friendly future fuel because it produces water as a combustion product; it is efficient, in addition to being inexhaustible and low cost compared to fossil fuels that cause severe damage to the environment.<sup>2</sup> Industrial pollutants such as organic dyes cause severe damage to the environment. Different processes such as adsorption, coagulation, and electrochemical are commonly used for their removal;<sup>2</sup> however, these methods do not have a leading role due to operational disadvantages.<sup>3</sup>

\*e-mail: giovanna.machado@cetene.gov.br

Editor handled this article: Fernando C. Giacomelli (Associate)



Semiconductor-based photocatalysis is a promising mechanism for solar energy harvesting and pollutant degradation. To obtain efficiency in the process, the semiconductor should have suitable band edges and visible light-harvesting characteristics and present chemical stability and photocorrosion resistance.<sup>4</sup> In addition to these features, the rapid recombination between photogenerated charge carriers (electron/hole pair- $e^-/h^+$ ) inhibits greater efficiency of different photocatalysts. To suppress the recombination, an alternative route is the formation of heterojunctions which helps decrease the recombination and improve charge transportation; thereby, resulting in greater efficiency.<sup>5</sup> In addition, depending on the composition and bandgaps of the semiconductors, one can synergize the electronic, optical, and structural properties of the semiconductors in the heterojunction for improved photocatalytic performance.<sup>6,7</sup>

Tantalum pentoxide ( $Ta_2O_5$ ) is a widely studied semiconductor for photocatalysis due to its excellent electronic and thermal properties and chemical stability.  $Ta_2O_5$  has a wide bandgap (3.9 eV, n-type) with an indirect transition which infers its photocatalytic activity once excited with the UV-Vis light.<sup>8</sup> However, due to the restricted absorption properties, structural modifications or semiconductor heterojunctions are needed to improve its performance.<sup>9</sup> Furthermore, due to 1D charge transportation nature and high aspect ratio, nanotubular  $Ta_2O_5$  morphology displays impressive photocatalytic performance.<sup>10</sup> In recent years, bismuth vanadate ( $BiVO_4$ , energy band gap ( $E_g$ ) = 2.4 eV, n-type) has drawn considerable attention in the photocatalysis field due to its visible light absorption, good dispersibility, non-toxicity, and corrosion resistance.<sup>11</sup>  $BiVO_4$ , due to lone pair distortion of Bi 6s orbital exhibits a greater photocatalytic performance in visible-light illumination. Additionally, the overlap of O 2p and Bi 6s orbitals in the valence band (VB) increases photocatalytic activity due to the mobility of photogenerated charge carriers.<sup>12</sup> However, low adsorptive capacity and difficulty in migration and separation of the photogenerated charge carriers are the bottlenecks towards its improved photocatalytic performance.<sup>13</sup> The interaction between  $Ta_2O_5$  and  $BiVO_4$  generates an n-n type heterojunction. For n-n type heterojunctions, the Fermi energies tend to balance to reach the same energy level, enabling the charge transfer between the semiconductors and improving the photocatalytic response of the proposed system.<sup>14</sup> This aspect is efficient in  $N_2$  fixation using g- $C_3N_4/Cu_3V_2O_8$  nanocomposites, in the photodegradation of organic compounds using  $BiOBr-Bi_2WO_6$ , as well as in the  $H_2$  production, using the  $WO_3/CoS_2$  heterojunction.<sup>15-17</sup>

It would be interesting to synergize the electronic and absorption properties of both semiconductors to improve the photocatalytic activities through forming an efficient heterostructure between them. It is important to note that the physical mixing of semiconductors may not truly result in the formation of an efficient heterostructure. It is due to non-uniformity and low adsorption at the interfaces inside the heterostructure.<sup>18</sup> In addition, controlling relative amounts of each photocatalyst is another important factor to obtain the synergy between the semiconductors.<sup>7</sup> Thus, efforts are necessary to develop techniques that enable the formation of efficient heterostructures.

To combine the photocatalytic potential and adsorptive capacity of  $Ta_2O_5$  synergistically with the optical properties of  $BiVO_4$ , this work investigates  $Ta_2O_5/BiVO_4$  heterojunction formation through a physical mixture between the semiconductors and also with a hydrothermal heat treatment, applying different molar ratios between the semiconductors. The photocatalysts are applied in the photodegradation of methylene blue (MB) and  $H_2$  production. To the best of our acknowledgment, this is the first work studying this n-n heterojunction.

## Experimental

### Chemicals

All chemicals were reagent grade and used without further purification. Tantalum plate (Ta, 99.98%, 0.25 mm thick) and potassium ferricyanide ( $K_3[Fe(CN)_6]$ , 99%) were purchased from Sigma-Aldrich (Santo André, Brazil). Potassium ferrocyanide ( $K_4[Fe(CN)_6]$ , 98.5%) was purchased from Êxodo (Sumaré, Brazil). Monoethylene glycol (MEG, 99%), fluoridric acid (HF, 40%), and acetone (99.5%) were acquired from Synth (Diadema, Brazil). Sulfuric acid ( $H_2SO_4$ , 37%) and hydrogen peroxide ( $H_2O_2$ , 50%) were purchased from Dinâmica (Indaiatuba, Brazil). Bismuth nitrate pentahydrate ( $Bi(NO_3)_3 \cdot 5H_2O$ , 98%) and ammonium metavanadate ( $NH_4VO_3$ , 99%) were purchased from Neon (Suzano, Brazil). Solvents and reagents of analytical grade were used as received. Water used in the syntheses and photocatalytic tests was of Milli-Q grade (18.2 M $\Omega$  cm).

### Synthesis of $Ta_2O_5$ nanotubes

The Ta plate (99.98%, 4.0 cm  $\times$  1.9 cm  $\times$  0.25 mm) was subjected to a previous cleaning, under low-power ultrasound (Ultracleaner 1600 A), with HF (40%) for 5 min, followed by dextran<sup>®</sup> (10% m/m), distilled water, and acetone for 10 min for each solvent.

During the anodization process, a DC power supply (Supplier AC power source) was used to provide a 50 V constant potential for 10 min. Ta and Cu plates were used as anode and cathode, respectively. The area of the electrodes was 15.2 cm<sup>2</sup> each, considering both sides of the Ta and Cu plates, the distance between the anode and the cathode was maintained at 1.0 cm. The electrolyte solution (72 mL) was composed of 95 wt.% of H<sub>2</sub>SO<sub>4</sub> and 5 wt.% of HF. Prior to the anodization, the electrochemical cell was immersed in a hot bath at 54 °C for 15 min to achieve thermal equilibrium and the anodization was conducted at a constant temperature of 54 °C and after anodization, the Ta/Ta<sub>2</sub>O<sub>5</sub> plates were sonicated for 60 min in Milli-Q water for the detachment of the Ta<sub>2</sub>O<sub>5</sub> nanotubes. The powder was centrifuged (10 mg *per* anodizing on average), dried at a constant temperature (60 °C/24 h), and heated in a furnace at 10 °C min<sup>-1</sup> rate up to 800, 850, and 900 °C during 4 h in an oxidizing atmosphere.

#### Hydrothermal synthesis of BiVO<sub>4</sub>

The BiVO<sub>4</sub> synthesis occurred through the co-precipitation method, followed by hydrothermal treatment. Typically, 20 mmol of Bi(NO<sub>3</sub>)<sub>3</sub>·5H<sub>2</sub>O (25 °C) and 20 mmol of NH<sub>4</sub>VO<sub>3</sub> (60 °C) were separately diluted in 25 mL of Milli-Q water under magnetic stirring for 30 min. After complete dissolution of Bi(NO<sub>3</sub>)<sub>3</sub> in water, the NH<sub>4</sub>VO<sub>3</sub> solution was slowly dripped into the Bi(NO<sub>3</sub>)<sub>3</sub> solution to form a yellowish BiVO<sub>4</sub> suspension. The pH of the solution was adjusted with a 0.1 mol L<sup>-1</sup> NaOH solution to values equal to 2.0, 3.5, and 5.0 and submitted to hydrothermal treatment at 180 °C for 6 h.<sup>19</sup>

#### Ta<sub>2</sub>O<sub>5</sub>/BiVO<sub>4</sub> heterostructure hydrothermal synthesis

For the Ta<sub>2</sub>O<sub>5</sub>/BiVO<sub>4</sub> heterojunction preparation, different molar ratios were studied between the semiconductors BiVO<sub>4</sub> and Ta<sub>2</sub>O<sub>5</sub> (0.5, Ta<sub>2</sub>O<sub>5</sub>/BiVO<sub>4</sub>-0.5H; 1.0, Ta<sub>2</sub>O<sub>5</sub>/BiVO<sub>4</sub>-1.0H; 2.0, Ta<sub>2</sub>O<sub>5</sub>/BiVO<sub>4</sub>-2.0H), previously synthesized. Amounts of 45 μmol of BiVO<sub>4</sub> and 22 μmol of Ta<sub>2</sub>O<sub>5</sub> (1:2 ratio) were added to 6 mL of Milli-Q water and the pH of the solution was adjusted to 2 using a 0.1 mol L<sup>-1</sup> HCl solution. The solution remained under magnetic stirring for 30 min. Subsequently, the produced suspension was added to a hydrothermal reactor and maintained at a constant temperature of 120 °C for 24 h. After cooling down, the heterojunction was centrifuged and dried at 80 °C for 3 h. A physical mixture of a 1:1 molar ratio between Ta<sub>2</sub>O<sub>5</sub> and BiVO<sub>4</sub> without hydrothermal treatment was used as a reference (Ta<sub>2</sub>O<sub>5</sub>/BiVO<sub>4</sub>-M), where the letters H and M represent hydrothermal and mechanical mixture,

respectively. For this, the samples were added to 10 mL of ethanol and kept under magnetic stirring for 24 h. At the end of the process, the solution was centrifuged, and the powder was dried at 80 °C for 3 h.

#### Photocatalytic performance analyses: MB photodegradation and H<sub>2</sub> production

The photocatalytic measurements were performed with a Newport simulator model 69907 equipped with a xenon (Xe) lamp with a maximum power of 300 W. Experiments were carried out under constant irradiation of 100 mW cm<sup>-2</sup>, calibrated by a photodiode with known responsiveness and with an 81094 AM 1.5 G filter.

For MB photodegradation experiments, 17 mL of a 15-ppm methylene blue solution were added to a quartz reactor together with 4.25 mg of the tested catalysts (Ta<sub>2</sub>O<sub>5</sub>, BiVO<sub>4</sub>, and Ta<sub>2</sub>O<sub>5</sub>/BiVO<sub>4</sub>). Initially, the suspension formed with the MB solution and the catalyst remained under magnetic stirring for 30 min in the absence of light, for the MB adsorption process onto the photocatalyst. Under excitation, MB was photodegraded for 180 min, whereas aliquots were taken every 30 min. The aliquots were centrifuged, and the concentration of the supernatant was monitored using an Agilent Cary 300 spectrophotometer (200-800 nm).

For the hydrogen evolution experiments, 4.25 mg of the catalysts were added to a quartz reactor containing 17 mL of a 0.03/0.12 mol L<sup>-1</sup> solution of Fe<sup>2+</sup>/Fe<sup>3+</sup> ions used as a hole scavenger system. The quartz reactor was sealed with a rubber septum and purged with argon gas for 30 min. The gaseous products were quantified by gas chromatography using an Agilent Model 7820A gas chromatograph (GC) with 30 m HP-PLOT/Q column and a 30 m HP-MOLESIEVE at room temperature. The generated gases were analyzed simultaneously with a thermal conductivity detector (TCD). Thus, for each time interval (30 min), a 450 μL aliquot was collected from the reactor headspace.

#### Characterization

The diffuse reflectance spectra of the semiconductors were obtained using a CARY 5000 UV-Vis spectrophotometer (Agilent Technologies) equipped with an integrating sphere, using BaSO<sub>4</sub> as reference. The spectral range was 200 to 800 nm with 1 nm of resolution. X-ray diffraction (XRD) patterns were taken on a Bruker X-ray diffractometer model D8 Advance with Cu Kα radiation (λ = 1.5418 Å) and with the 2θ range from 10 to 80° with a step of 0.02°. The scanning electron microscopy (SEM) images were

obtained using an FEI Quanta 200F field emission scanning electron microscope (FESEM) coupled with electron probe energy-dispersive X-ray spectrometer (EDX) for EDS mapping surface. The transmission electron micrographs were recorded with an FEI TECNAI G2 high-resolution transmission electron microscope (HRTEM) at 200 kV. For HRTEM analysis the samples were prepared by dispersing freestanding semiconductor powders in isopropanol at room temperature. One drop was deposited on a 400-mesh holey carbon-coated Cu grid. Raman spectra were obtained with an Ocean Optics QE65000 spectrometer with a 785 nm Ar-Kr laser.

## Results and Discussion

### Synthesis and characterization of photocatalysts

The synthesis of Ta<sub>2</sub>O<sub>5</sub> nanotubes was monitored in real-time through the photocurrent density curve (J) vs. time (t) (Figure S1, Supplementary Information (SI) section). The J-t curve matches well with the previously obtained curves for Ta<sub>2</sub>O<sub>5</sub> anodization.<sup>20</sup> The as-synthesized Ta<sub>2</sub>O<sub>5</sub> nanotubes were heat-treated to increase the degree of structural order. The increase in crystallinity is important

as it tends to decrease the recombination rate and makes the material more efficient in photocatalytic processes.<sup>21</sup> In the literature, the orthorhombic phase of Ta<sub>2</sub>O<sub>5</sub> was observed at temperatures from 750 °C, having an increase in crystallinity up to the temperature of 900 °C. Further increasing the temperature resulted in the structural collapse of the nanotubes.<sup>20,22,23</sup>

The morphology of the samples was analyzed using SEM (Figure 1). As observed earlier in the literature, the morphologies of the Ta<sub>2</sub>O<sub>5</sub> nanotubes were sustained even after the thermal treatment at 800 °C (Figure 1a), 850 °C (Figure 1b), and 900 °C (Figure 1c).<sup>10,23</sup> Overall, for the Ta<sub>2</sub>O<sub>5</sub> sample heat-treated at 900 °C, the nanotubes have an approximate length of 7.6 μm and diameter of 100 nm (Figure S2a, SI section). Figure S2b shows the energy-dispersive X-ray (EDX) spectra and elemental composition of the synthesized Ta<sub>2</sub>O<sub>5</sub> annealed at 900 °C. The main spectroscopic peaks for Ta<sub>2</sub>O<sub>5</sub> nanotubes were: 0.27 KeV (C K<sub>α</sub>), 0.52 KeV (O K<sub>α</sub>), 1.72 KeV (Ta M<sub>α</sub>), 8.15 KeV (Ta L<sub>α</sub>), and 9.34 KeV (Ta L<sub>β</sub>). Figure 1d shows the X-ray diffraction (XRD) patterns for the Ta<sub>2</sub>O<sub>5</sub> nanotubes synthesized at different temperatures. The diffractograms show peaks at 22.8, 28.4, 36.7, 46.7, 49.8, and 55.5°, corresponding to the planes (100), (0111), (1111), (200),

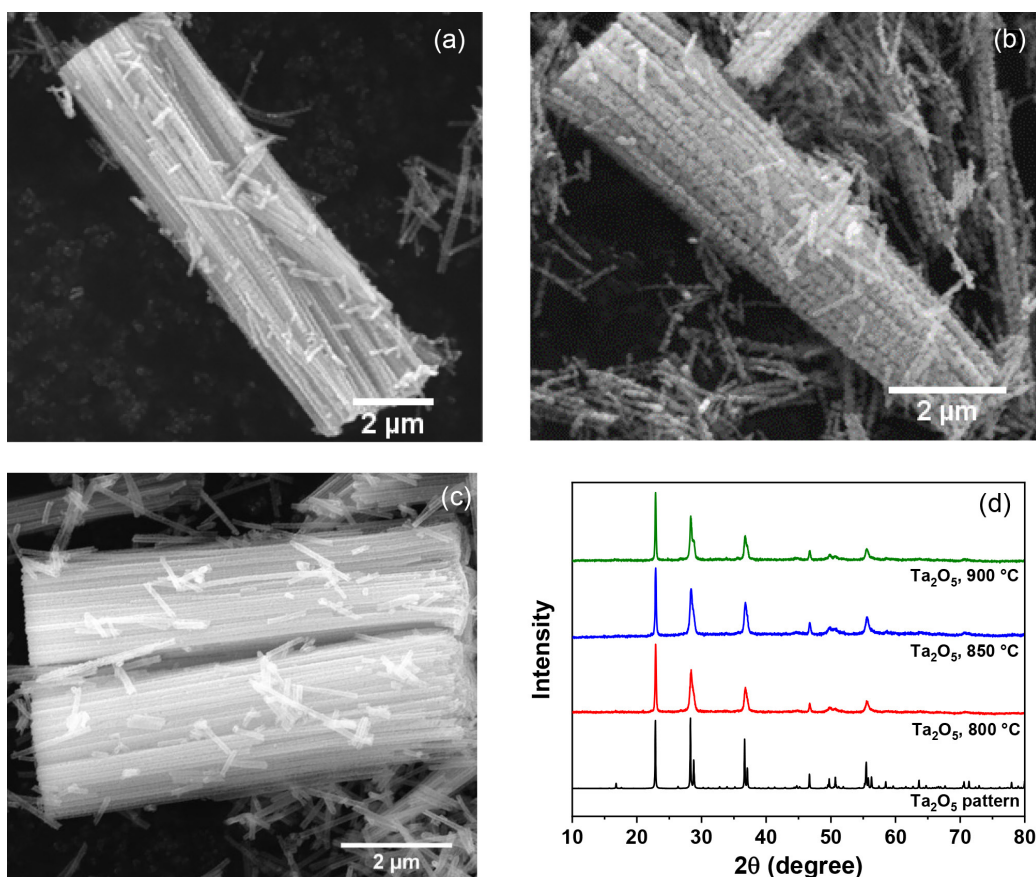


**Figure 1.** SEM image of Ta<sub>2</sub>O<sub>5</sub> nanotubes heat-treated at (a) 800 °C, (b) 850 °C, and (c) 900 °C. (d) XRD patterns for Ta<sub>2</sub>O<sub>5</sub> nanotubes.

(0220), and (2111) of the orthogonal phase (COD: 2106064); confirming a complete formation of crystalline Ta<sub>2</sub>O<sub>5</sub>.<sup>24</sup> The better definition of the diffraction peaks presented between 28.0 and 29.0° (Figure 1d), because of the temperature increase (800 to 900 °C). This fact suggests a better structural arrangement of the produced nanotubes.

The UV-Vis absorption spectra of the Ta<sub>2</sub>O<sub>5</sub> nanotubes were obtained by diffuse reflectance spectroscopy (DRS), using the Kubelka-Munk function.<sup>25</sup> Nanotubes obtained through different heat treatment temperatures show similar optical absorption behavior (Figure S3, SI section), with an intense absorption band ( $\lambda_{\text{onset}} = 280\text{-}310$  nm) for all samples. The bathochromic shift in the spectrum of the crystalline Ta<sub>2</sub>O<sub>5</sub> compared to that of the amorphous nanotubes (Figure S3) depicts the better optical absorption of the solar spectrum for crystalline Ta<sub>2</sub>O<sub>5</sub> nanotubes. The bandgap energy of Ta<sub>2</sub>O<sub>5</sub> was determined by the Tauc plots ( $(\alpha h\nu)^{1/r}$  vs.  $h\nu$ ) (Figure 2), where  $\alpha$  is the absorption coefficient,  $h$  is the Planck constant and  $\nu$  is the light frequency.<sup>26</sup> Ta<sub>2</sub>O<sub>5</sub> exhibits indirect allowed electronic transition ( $r = 2$ ).<sup>27</sup> The estimated bandgap energy for the Ta<sub>2</sub>O<sub>5</sub> nanotubes was 4.10, 3.89, 3.84, and 3.85 eV for the amorphous nanotubes and those treated at 800, 850, and 900 °C, respectively. The cause of the decrease in the band gap energy of Ta<sub>2</sub>O<sub>5</sub> with the heat treatment is due to the change from the amorphous to the orthogonal structure.<sup>28</sup>

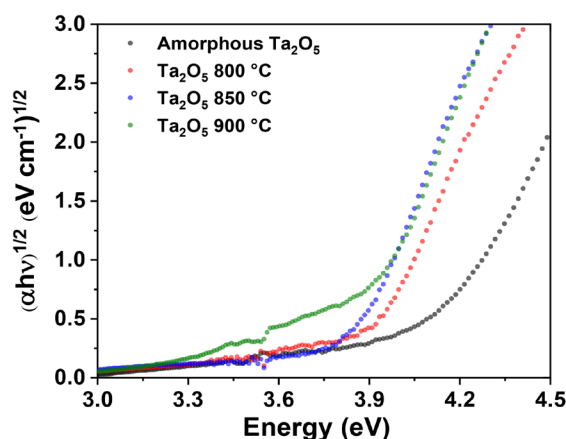


**Figure 2.** Tauc plot for the amorphous nanotubes and those treated at 800, 850, and 900 °C, respectively.

BiVO<sub>4</sub> synthesis was controlled by pH adjustment before hydrothermal treatment at 180 °C for 6 h without the support of stabilizers. The synthesis occurs through the interaction of Bi<sup>3+</sup> cations with vanadium precursors in an aqueous solution. The VO<sub>4</sub><sup>3-</sup> ions are stable only in a highly basic medium. After the acidification of the medium, they undergo polymerization, forming VO<sub>4</sub> tetrahedrons connected by corners, developing the species [V<sub>2</sub>O<sub>7</sub>]<sup>4-</sup>, [V<sub>4</sub>O<sub>12</sub>]<sup>4-</sup>, [V<sub>3</sub>O<sub>9</sub>]<sup>3-</sup>, [V<sub>10</sub>O<sub>28</sub>]<sup>6-</sup>, and [VO]<sup>2+</sup>.<sup>29,30</sup>

Metavanadates produce BiVO<sub>4</sub> at different pH conditions, however, hydrothermal treatment is necessary for the production of nanosystems with phase purity.<sup>31</sup>

BiVO<sub>4</sub> morphology was evaluated using SEM (Figures 3a-3c). The hexagon-like morphology is observed in the SEM image (Figure 3), being observed plates with polydispersion of sizes. Figure 3d displays the XRD patterns for the BiVO<sub>4</sub> samples. The BiVO<sub>4</sub> diffractograms show peaks at 29.0, 30.5, 34.5, 35.3, 39.8, 42.5, 46.8, 47.3, 50.2, 53.3, 58.4, and 59.5°, corresponding to the planes (121), (040), (200), (002), (141), (051), (240), (042), (202), (161), (321), and (123) of the monoclinic clinobisvanite phase (scheelite-type structure) (COD: 9013437) for the samples prepared at pH values of 2.0, 3.5 and 5.0.<sup>32,33</sup> The narrow peaks suggest the highly crystalline nature of the obtained BiVO<sub>4</sub>. The tetragonal structure is characterized by the presence of a single peak at 35°,<sup>34</sup> whereas in the patterns of Figure 3e, two peaks are observed at 34.5 and 35.3°, evidencing the pure monoclinic phase of all prepared BiVO<sub>4</sub> samples.<sup>33</sup>

UV-Vis DRS spectra were recorded for the precipitate before hydrothermal treatment and the BiVO<sub>4</sub> samples prepared at pH values of 2.0, 3.5, and 5.0, followed by hydrothermal treatment. The spectrum of the amorphous BiVO<sub>4</sub> sample (Figure S4, SI section) presents an absorption continuum in the visible region with low intensity and intense band in the UV region, with maxima at 230 and 278 nm. After the hydrothermal treatment, broadened light absorptions towards visible light were observed in all cases, with onsets close to 500 nm. The fundamental electronic transition of BiVO<sub>4</sub> is classified as indirect with a value equal to 2.5 eV, also having a direct transition of 2.7 eV.<sup>27</sup> The Tauc plot (Figure 4a) was applied to determine the bandgap energy of the BiVO<sub>4</sub>. The BiVO<sub>4</sub> presented bandgap energies of 2.13, 2.37, 2.41, and 2.42 eV for amorphous and heat-treated materials at pH 2.0, 3.5, and 5.0, respectively. Despite the enhancement in bandgap energy after hydrothermal treatment (180 °C, 6 h), the significant increase in optical absorption makes the material much more active for photocatalytic processes. In addition, the indirect transition nature of BiVO<sub>4</sub> makes the charge carriers relaxation time longer and the direct transition ensures greater light absorption, making BiVO<sub>4</sub> an impressive semiconductor applied in photocatalysis.<sup>35</sup>

Raman spectra were acquired in the range of 0-1000 cm<sup>-1</sup> to study the vibrational characteristics of BiVO<sub>4</sub> (Figure 4b). For sample synthesized at pH 2.0, 3.5, and 5.0, Raman bands are observed at 329, 370, 741, and 829 cm<sup>-1</sup>. At 329 and 370 cm<sup>-1</sup>, the symmetrical (A<sub>g</sub> symmetry) and asymmetrical (B<sub>g</sub> symmetry) bending modes of the vanadate anion (VO<sub>4</sub><sup>3-</sup>) are observed. The strongest stretch,

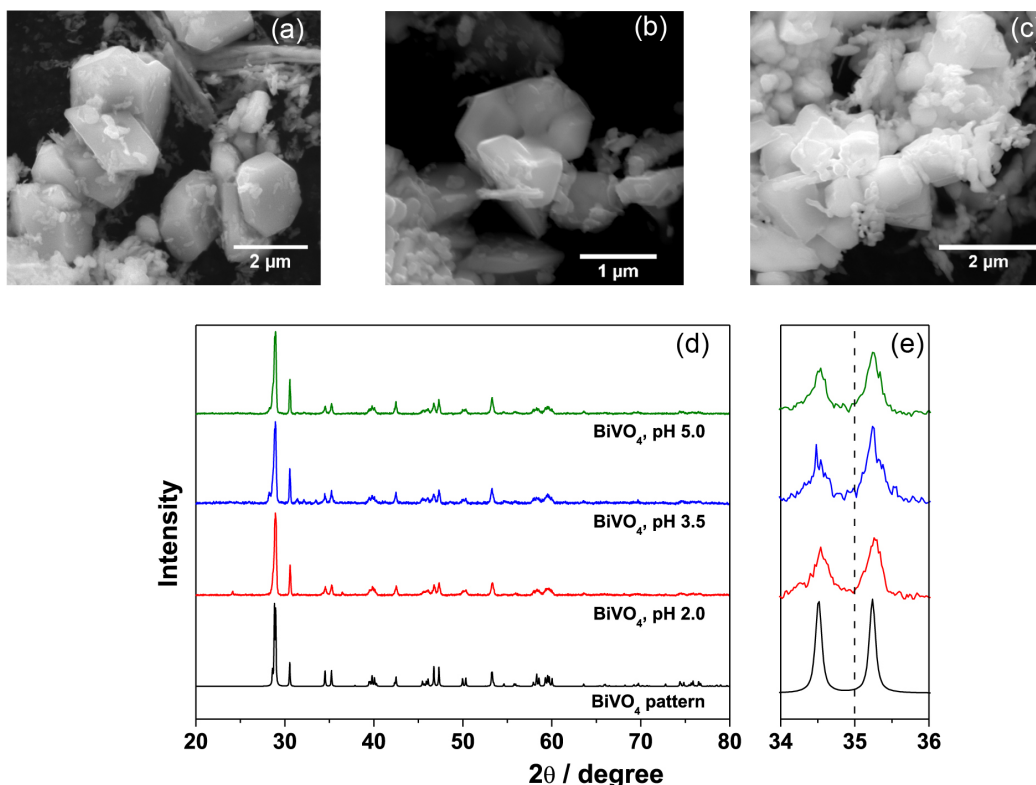


**Figure 3.** SEM image of  $\text{BiVO}_4$  synthesized at (a) pH 2.0, (b) 3.5, and (c) 5.0. (d) XRD diffraction patterns and (e) magnified view between  $34$  and  $36^\circ$  for  $\text{BiVO}_4$  synthesized at pH 2.0, 3.5, and 5.0.

at  $826\text{ cm}^{-1}$ , is associated with the symmetrical stretching of the V–O connection ( $A_g$  symmetry) while at  $741\text{ cm}^{-1}$  the asymmetric stretching is present ( $B_g$  symmetry). In the Raman spectrum, the position of the bands is sensitive to short-range orders, while the full width at half maximum (FWHM) of the bands are sensitive to the crystallinity degree, defects and disorders, particle size, and aggregation.<sup>31</sup> The pH 2.0, 3.5 and 5.0 systems have their most intense Raman band at  $828$ ,  $831$ , and  $832\text{ cm}^{-1}$  (Figure 4c) while the FWHM of these bands presents values equal to  $52.1$ ,  $49.5$ , and  $52.4\text{ cm}^{-1}$ , respectively. Thus,  $\text{BiVO}_4$  prepared at pH 2.0 has short-range mean symmetry of regular  $\text{VO}_4$  tetrahedrons, while the pH 3.5 sample present the highest crystallinity and consequently fewer defects.

The photocatalytic performances for the photodegradation of dyes of the prepared semiconductors were evaluated through MB degradation under simulated solar irradiation. The MB photodegradation procedure was performed through an adsorption period of 30 min in the dark, followed by 180 min of monitoring under irradiation, with aliquots removed every 30 min. MB in the absence of photocatalyst has low UV-Vis photodegradation (Figure S5a, SI section), degrading only 7.0% after 180 min of irradiation (Figure 5).  $\text{Ta}_2\text{O}_5$  (Figure 5a) and  $\text{BiVO}_4$  (Figure 5b) were applied separately as photocatalysts, showing effective photodegradation after 180 min of

irradiation.  $\text{Ta}_2\text{O}_5$  presents a large bandgap, as observed in the Tauc plot when compared to  $\text{BiVO}_4$  (Figures 2 and 4a), so the limited absorption of the solar spectrum by  $\text{Ta}_2\text{O}_5$  nanotubes ( $< 300\text{ nm}$ , Figure S3) reduces its efficiency when compared to  $\text{BiVO}_4$ .  $\text{Ta}_2\text{O}_5$  presents a 21, 22, and 30% reduction in MB concentration for the samples heat-treated at the temperatures of  $800^\circ\text{C}$  (Figure S5b),  $850^\circ\text{C}$  (Figure S5c) and  $900^\circ\text{C}$  (Figure S5d), respectively.  $\text{BiVO}_4$  reduces the MB concentration by 45, 40, and 30% for the synthesis conditions at pH 2.0 (Figure S6a, SI section), 3.5 (Figure S6b), and 5.0 (Figure S6c).

The pseudo-first-order reaction kinetic model of  $\text{Ta}_2\text{O}_5$  (Figure S7a, SI section) and  $\text{BiVO}_4$  (Figure S7b) quantitatively presents the reaction kinetics of MB degradation.<sup>36</sup> The model is defined through equation 1:

$$\ln(C_0/C) = kt \quad (1)$$

where  $C_0$  and  $C$  are the initial MB concentration and the concentration at time  $t$ , respectively. The term  $k$  is the first-order rate constant and  $t$  is the irradiation time. The values obtained through the linear adjustment of the curves for  $\text{Ta}_2\text{O}_5$  and  $\text{BiVO}_4$  are shown in Table S3, SI section. Constant  $k$  values indicate better photocatalytic performance for  $\text{Ta}_2\text{O}_5$  heat-treated at  $900^\circ\text{C}$  ( $1.11 \times 10^{-3}\text{ min}^{-1}$ , Table S3, entry 4) and  $\text{BiVO}_4$  synthesized at pH 2.0 ( $3.29 \times 10^{-3}$ ,

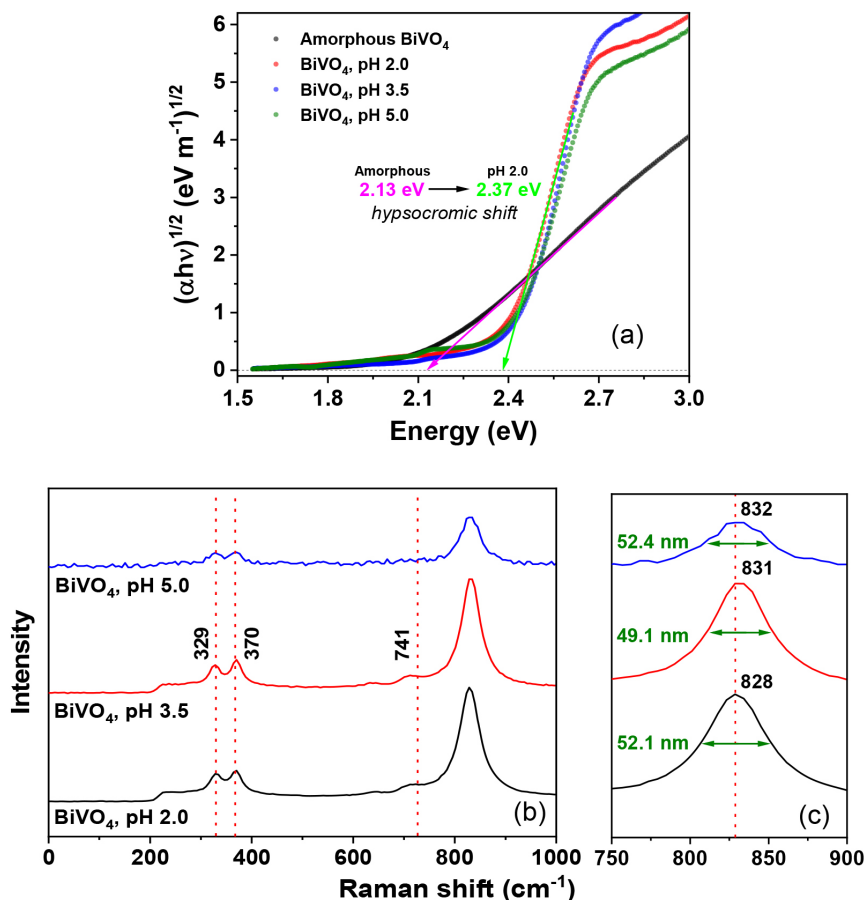


Figure 4. (a) Tauc plot and (b) Raman spectra for BiVO<sub>4</sub> synthesized at pH 2.0, 3.5, and 5.0. (c) In detail: 750-900 cm<sup>-1</sup> for Raman spectra.

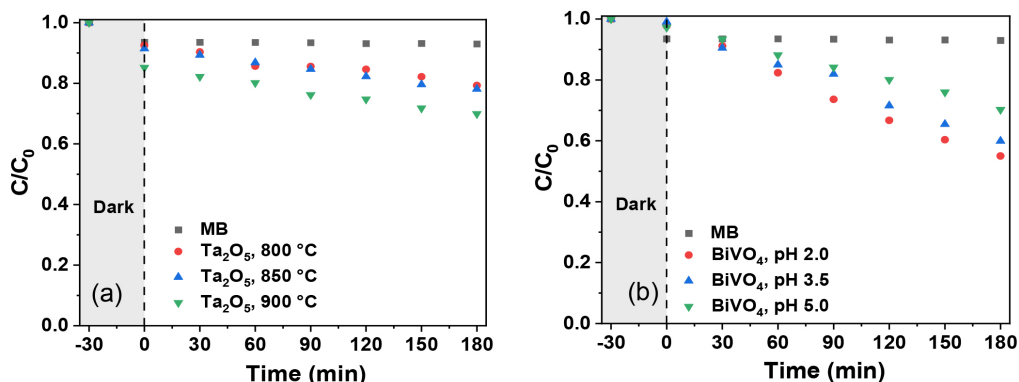


Figure 5. Photocatalytic curves of (a) Ta<sub>2</sub>O<sub>5</sub> nanotubes (800, 850, and 900 °C) and (b) BiVO<sub>4</sub> (pH 2.0, 3.5, and 5.0).

Table S3, entry 5). The increase in temperature provides better photocatalytic activity for Ta<sub>2</sub>O<sub>5</sub> due to the improvement in the structural arrangement of the obtained nanotubes, as observed in XRD patterns (Figure 1d). BiVO<sub>4</sub> produced at pH 2.0 is the one with the highest crystallinity and the lowest number of defects, as indicated by Raman spectroscopy (Figure 4b).

The photocatalytic performance of heterojunctions is linked to the crystallinity and low density of structural defects of the semiconductors that constitute it.<sup>25</sup>

The best individual performance samples were the Ta<sub>2</sub>O<sub>5</sub> nanotubes heat-treated at 900 °C and BiVO<sub>4</sub> synthesized at pH 2.0, being chosen for the production of heterojunctions. Literature preceding reports on changes in BiVO<sub>4</sub> crystalline phase at harsh acidic conditions. Using hydrothermal treatment at pH 1.7, Zhang *et al.*<sup>31</sup> obtained the tetragonal phase and demonstrated that the tetragonal phase is not efficient for photochemical reactions when compared to the monoclinic phase of BiVO<sub>4</sub>. The monoclinic phase was obtained preferentially

by increasing the basicity of the reaction medium. In this work, we obtained monoclinic structures, at pH 2.0, 3.5 and 5.0 where the synthesis conducted at pH 2.0 presented the best performance. For the preparation of the  $\text{Ta}_2\text{O}_5/\text{BiVO}_4$  heterostructure, a mechanical mixture was subjected to hydrothermal treatment for better interaction between the surface of the semiconductors, being used ratios between the semiconductors  $\text{Ta}_2\text{O}_5$  and  $\text{BiVO}_4$  equal to 0.5 ( $\text{Ta}_2\text{O}_5/\text{BiVO}_4$ -0.5H), 1.0 ( $\text{Ta}_2\text{O}_5/\text{BiVO}_4$ -1.0H) and 2.0 ( $\text{Ta}_2\text{O}_5/\text{BiVO}_4$ -2.0H). The pH applied during the hydrothermal treatment was adjusted to 2.0 to maximize the efficiency of the  $\text{Ta}_2\text{O}_5/\text{BiVO}_4$  heterostructure, justified by its sensitivity to heat treatment pH in its photocatalytic performance (Figure 5b). For comparison criteria, a mechanical mixture ( $\text{Ta}_2\text{O}_5/\text{BiVO}_4$ -M) without hydrothermal treatment between semiconductors  $\text{Ta}_2\text{O}_5$  and  $\text{BiVO}_4$  was prepared, with a molar ratio equal to 1.0.

The studied heterojunctions were initially investigated by SEM (Figures 6a-6d). Mechanical mixing produces a physical approximation between semiconductors (Figure 6a), but without an apparent adhesion on their surfaces. For samples treated via hydrothermal conditions, it is possible to see the  $\text{BiVO}_4$  crystals decorated with  $\text{Ta}_2\text{O}_5$  grains for the sample of  $\text{Ta}_2\text{O}_5/\text{BiVO}_4$ -0.5H (Figure 6b),  $\text{Ta}_2\text{O}_5/\text{BiVO}_4$ -1.0H (Figure 6c) and  $\text{Ta}_2\text{O}_5/\text{BiVO}_4$ -2.0H (Figure 6d). A better interface between semiconductors can decrease excitonic recombination, being beneficial for the application of heterojunction in photocatalysis. XRD analyses (Figure 6e) present the characteristic

peaks described for  $\text{Ta}_2\text{O}_5$  (COD: 2106064) and  $\text{BiVO}_4$  (COD: 9013437).<sup>24,37</sup>

Raman spectroscopy was applied in the characterization of heterojunctions (Figure 6f). The band observed at  $78\text{ cm}^{-1}$  is related to the interaction between the Ta polyhedron and  $\text{Ta}_2\text{O}_n^{5-2n}$  and/or  $\text{Ta}_6\text{O}_{12}^{6+}$ . Transitions between  $100 < n < 450\text{ cm}^{-1}$  refer to O-Ta-O bending vibrations of  $\text{TaO}_6$  octahedra, where bands are presented for  $\text{Ta}_2\text{O}_5$  at 106 and  $130\text{ cm}^{-1}$ . Bands are also observed at 645 and  $710\text{ cm}^{-1}$ , regarding the stretching of the Ta-O bonds present in the  $\text{Ta}_2\text{O}_5$  nanotubes.<sup>38,39</sup> Other bands are also identified at 327, 369, and  $828\text{ cm}^{-1}$  (Figure 6f), as presented for  $\text{BiVO}_4$  (Figure 4b). The UV-Vis reflectance spectra of the samples  $\text{Ta}_2\text{O}_5/\text{BiVO}_4$ -M,  $\text{Ta}_2\text{O}_5/\text{BiVO}_4$ -0.5H,  $\text{Ta}_2\text{O}_5/\text{BiVO}_4$ -1.0H, and  $\text{Ta}_2\text{O}_5/\text{BiVO}_4$ -2.0H have similar profiles (Figure 6g), with absorption bands centered at 265 and 460 nm, referring to  $\text{Ta}_2\text{O}_5$  and  $\text{BiVO}_4$ , respectively. The different intensities observed in the diffractogram (Figure 6e) and in the reflectance spectra (Figure 6g) refer to the molar ratios between  $\text{Ta}_2\text{O}_5$  and  $\text{BiVO}_4$  for each studied heterojunction.

The photocatalytic performance of the mechanical mixture ( $\text{Ta}_2\text{O}_5/\text{BiVO}_4$ -M) was evaluated in MB photodegradation (Figure 7a). As compared to pure  $\text{BiVO}_4$  (Figure 5b), this mixture resulted in a worse photodegradation performance (Table S3), reflecting the need for an alternative methodology to form efficient heterojunctions. Thus, we employed the hydrothermal method to form the heterojunction at different conditions

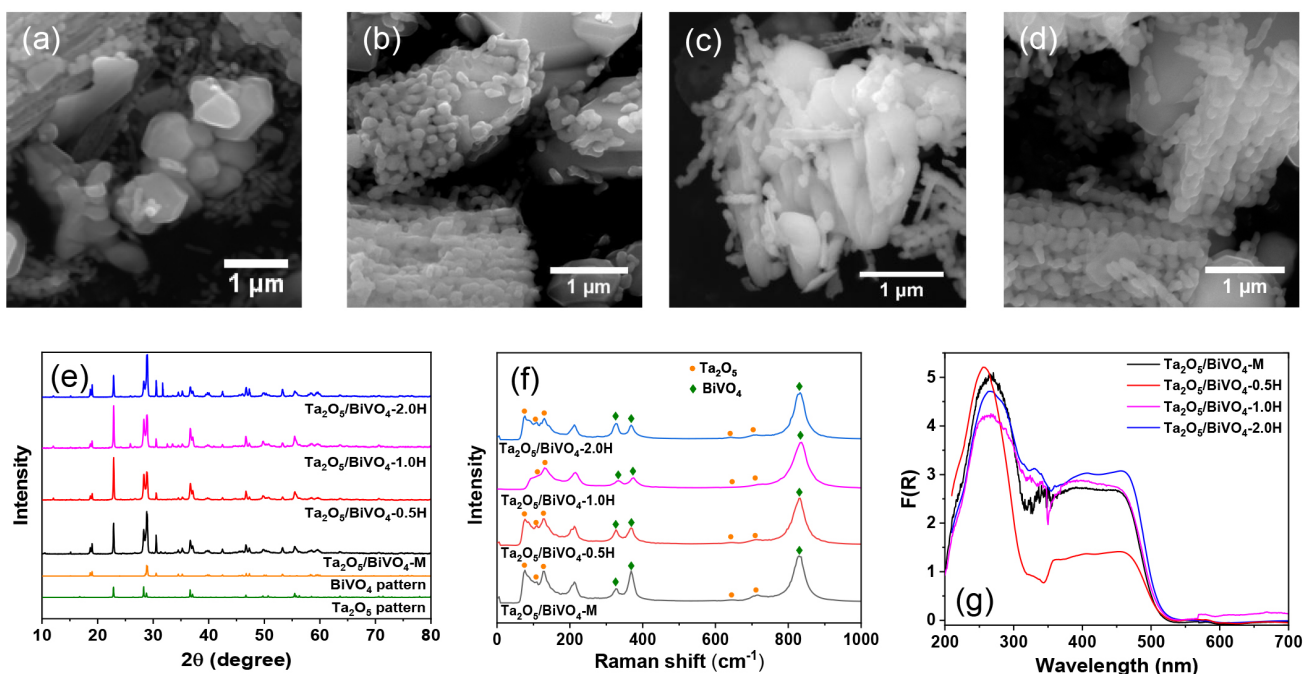


**Figure 6.** SEM image of (a)  $\text{Ta}_2\text{O}_5/\text{BiVO}_4$ -M, (b)  $\text{Ta}_2\text{O}_5/\text{BiVO}_4$ -0.5H, (c)  $\text{Ta}_2\text{O}_5/\text{BiVO}_4$ -1.0H, and (d)  $\text{Ta}_2\text{O}_5/\text{BiVO}_4$ -2.0H. (e) XRD pattern, (f) Raman spectra and (g) DRS spectra of  $\text{Ta}_2\text{O}_5/\text{BiVO}_4$ -M,  $\text{Ta}_2\text{O}_5/\text{BiVO}_4$ -0.5H,  $\text{Ta}_2\text{O}_5/\text{BiVO}_4$ -1.0H and  $\text{Ta}_2\text{O}_5/\text{BiVO}_4$ -2.0H.

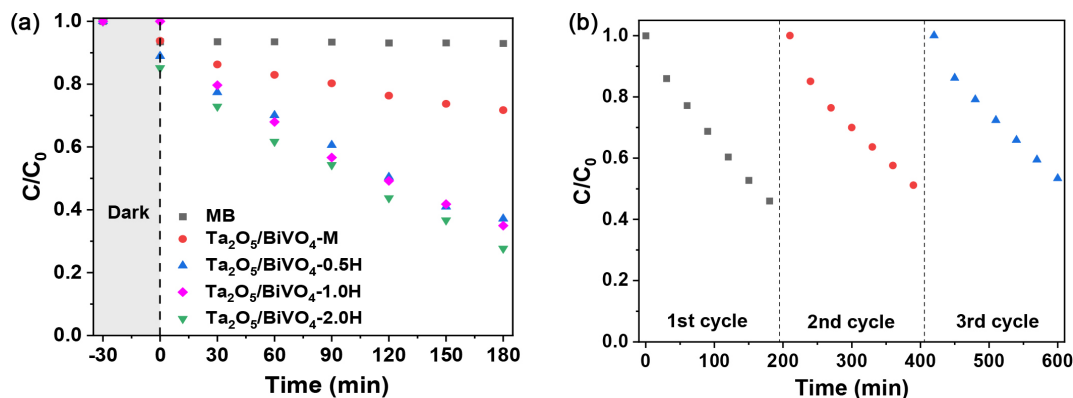


**Figure 7.** (a) Photocatalytic curves of Ta<sub>2</sub>O<sub>5</sub>/BiVO<sub>4</sub>-M, Ta<sub>2</sub>O<sub>5</sub>/BiVO<sub>4</sub>-0.5H, Ta<sub>2</sub>O<sub>5</sub>/BiVO<sub>4</sub>-1.0H and Ta<sub>2</sub>O<sub>5</sub>/BiVO<sub>4</sub>-2.0H. (b) Reuse cycles of Ta<sub>2</sub>O<sub>5</sub>/BiVO<sub>4</sub>-2.0H for MB photodegradation.

(Ta<sub>2</sub>O<sub>5</sub>/BiVO<sub>4</sub>-M, 0.5H, 1.0H and 2.0H) and tested them in MB photodegradation (Figure 7a).

Comparing the heterojunctions, Ta<sub>2</sub>O<sub>5</sub>/BiVO<sub>4</sub>-M decomposed 28.3% of the MB within 180 min, while Ta<sub>2</sub>O<sub>5</sub>/BiVO<sub>4</sub>-0.5H degrades 62.9%, Ta<sub>2</sub>O<sub>5</sub>/BiVO<sub>4</sub>-1.0H 65.1% and Ta<sub>2</sub>O<sub>5</sub>/BiVO<sub>4</sub>-2.0H 72.3%. These results demonstrate that mixing both semiconductors through a hydrothermal approach is an effective route for heterojunction formation. The reusability of the catalyst was evaluated through three MB photodegradation cycles during a period of 3 h each. As seen in Figure 7b, at the end of the 2<sup>nd</sup> and 3<sup>rd</sup> cycle, 90.1 and 86.4% of the photocatalytic performance are maintained.

Via pseudo-first-order reaction kinetic model of Ta<sub>2</sub>O<sub>5</sub>/BiVO<sub>4</sub> heterojunctions (Figure S8, SI section), the photocatalytic performance of MB degradation was analyzed. Data are shown in Table 1. The Ta<sub>2</sub>O<sub>5</sub>/BiVO<sub>4</sub>-2.0H heterojunction, with *k* equal to 6.06 × 10<sup>-3</sup> min<sup>-1</sup> (Table 1, entry 5) presents superior performance as compared to Ta<sub>2</sub>O<sub>5</sub>/BiVO<sub>4</sub>-0.5H (Table 1, entry 3) and Ta<sub>2</sub>O<sub>5</sub>/BiVO<sub>4</sub>-M (Table 1, entry 2). The effective formation of the heterojunction enables significant improvements in the photocatalytic properties of the material. The mechanical mixture between Ta<sub>2</sub>O<sub>5</sub> and BiVO<sub>4</sub> (Ta<sub>2</sub>O<sub>5</sub>/BiVO<sub>4</sub>-M) does not show significant improvement, due to the individual

action of each semiconductor. The hydrothermal treatment allows better interfacial contact between semiconductors, as observed through SEM images (Figures 6b-6d), justifying the higher value of *k*.<sup>19,40</sup>

By absorbing electromagnetic radiation, Ta<sub>2</sub>O<sub>5</sub>/BiVO<sub>4</sub> is excited producing charge carriers, as electrons in the conduction band (e<sup>-</sup><sub>CB</sub>) and holes in the valence band (h<sup>+</sup><sub>VB</sub>) (equation 2). The proposed MB photodegradation mechanism is divided into two steps, occurring simultaneously. Firstly, the photogenerated electrons react with the O<sub>2</sub> adsorbed in the heterojunction, producing the superoxide ion (O<sub>2</sub><sup>-•</sup>) (equation 3). In the second step, the holes are captured by water in the solution, producing the hydroxyl radicals (OH<sup>•</sup>) (equation 4). O<sub>2</sub><sup>-•</sup> and OH<sup>•</sup> species are highly reactive, acting directly on the photodegradation of MB (equations 5 and 6).<sup>41</sup>

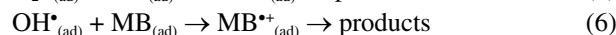
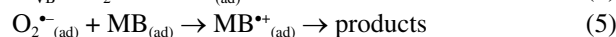
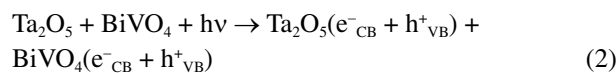


**Table 1.** The pseudo-first-order rate constant (*k*) of MB photodegradation on Ta<sub>2</sub>O<sub>5</sub>/BiVO<sub>4</sub>-M, Ta<sub>2</sub>O<sub>5</sub>/BiVO<sub>4</sub>-0.5H, Ta<sub>2</sub>O<sub>5</sub>/BiVO<sub>4</sub>-1.0H, and Ta<sub>2</sub>O<sub>5</sub>/BiVO<sub>4</sub>-2.0H

entry	Sample	<i>k</i> / min <sup>-1</sup>	R <sup>2</sup>
1	without photocatalyst	3.55 × 10 <sup>-5</sup>	0.89616
2	Ta <sub>2</sub> O <sub>5</sub> /BiVO <sub>4</sub> -M	1.43 × 10 <sup>-3</sup>	0.97544
3	Ta <sub>2</sub> O <sub>5</sub> /BiVO <sub>4</sub> -0.5H	5.02 × 10 <sup>-3</sup>	0.98981
4	Ta <sub>2</sub> O <sub>5</sub> /BiVO <sub>4</sub> -1.0H	5.30 × 10 <sup>-3</sup>	0.99681
5	Ta <sub>2</sub> O <sub>5</sub> /BiVO <sub>4</sub> -2.0H	6.06 × 10 <sup>-3</sup>	0.98793

R<sup>2</sup>: coefficient of determination.

In photocatalytic water splitting, despite better absorption in the visible region, BiVO<sub>4</sub> has poor electron transport and inadequate conduction band position to produce H<sub>2</sub>; however, it is promising for O<sub>2</sub> production; therefore, it has not been individually tested for H<sub>2</sub> production.<sup>42</sup> Firstly, we used Ta<sub>2</sub>O<sub>5</sub> for H<sub>2</sub> production (Figure S9, SI section). The production rate is sensitive to the heat treatment temperature of Ta<sub>2</sub>O<sub>5</sub> nanotubes, with a production of 4.26, 5.97, and 6.82 μmol g<sup>-1</sup> for nanotubes thermally treated at temperatures of 800, 850, and 900 °C, respectively. The hydrogen production results presented are further evidence of crystallinity improvement with higher heat treatment temperatures for Ta<sub>2</sub>O<sub>5</sub>. Furthermore, 900 °C

was also the optimal heat treatment for MB degradation (Figure 5).

After obtaining the optimal condition of MB degradation and H<sub>2</sub> production of individual semiconductors, we applied the Ta<sub>2</sub>O<sub>5</sub>/BiVO<sub>4</sub> heterostructure in photochemical hydrogen generation (Figure 8). Ta<sub>2</sub>O<sub>5</sub>/BiVO<sub>4</sub>-M, Ta<sub>2</sub>O<sub>5</sub>/BiVO<sub>4</sub>-0.5H, and Ta<sub>2</sub>O<sub>5</sub>/BiVO<sub>4</sub>-2.0H resulted in 2.80, 4.09, and 10.2 μmol g<sup>-1</sup>, respectively. As the total mass of applied catalyst was the same in all experiments, the Ta<sub>2</sub>O<sub>5</sub>/BiVO<sub>4</sub>-M sample, for presenting a 1:1 molar ratio between Ta<sub>2</sub>O<sub>5</sub> and BiVO<sub>4</sub>, presents a drop of 52.5% compared to pure Ta<sub>2</sub>O<sub>5</sub>, due to a reduction in the amount of Ta<sub>2</sub>O<sub>5</sub> in the catalyst mass. This result demonstrates the ineffectiveness of BiVO<sub>4</sub> in H<sub>2</sub> production and the absence of an effective interface between Ta<sub>2</sub>O<sub>5</sub> and BiVO<sub>4</sub> in the physical mixture. For Ta<sub>2</sub>O<sub>5</sub>/BiVO<sub>4</sub>-M sample, Ta<sub>2</sub>O<sub>5</sub> is individually responsible for the H<sub>2</sub> production. The hydrothermal treatment favors the formation of active heterojunctions, being the Ta<sub>2</sub>O<sub>5</sub>/BiVO<sub>4</sub>-2.0H the most efficient in H<sub>2</sub> production (Figure 7). Ta<sub>2</sub>O<sub>5</sub>/BiVO<sub>4</sub>-0.5H and Ta<sub>2</sub>O<sub>5</sub>/BiVO<sub>4</sub>-2.0H present grains of Ta<sub>2</sub>O<sub>5</sub> on the surface of the BiVO<sub>4</sub> (Figures 6b and 6d). However, Ta<sub>2</sub>O<sub>5</sub>/BiVO<sub>4</sub>-2.0H has greater absorption in the visible region (higher content

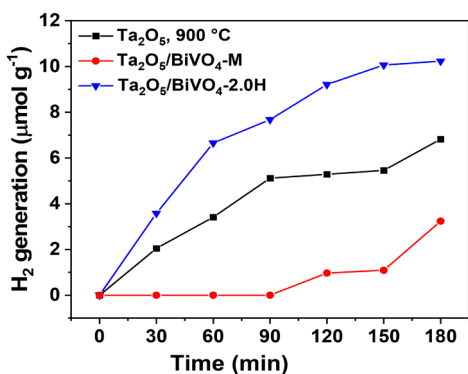


**Figure 8.** Photocatalytic H<sub>2</sub> evolution of Ta<sub>2</sub>O<sub>5</sub> 900 °C, Ta<sub>2</sub>O<sub>5</sub>/BiVO<sub>4</sub>-M and Ta<sub>2</sub>O<sub>5</sub>/BiVO<sub>4</sub>-2.0H.

of BiVO<sub>4</sub>) (Figure 6g), which maximizes light absorption and the number of electrons/holes involved in the photochemical process.

Based on Mulliken's theoretical method of absolute electronegativity, we determined the relative energy levels of the bands referring to the Ta<sub>2</sub>O<sub>5</sub> and BiVO<sub>4</sub> semiconductors (details in SI section) before the heterojunction formation (Figure 9a). It is reported that BiVO<sub>4</sub> and Ta<sub>2</sub>O<sub>5</sub> are n-type semiconductors.<sup>10,43</sup> With the heterojunction formation, there is an alignment of Fermi energies (E<sub>F</sub>) at the interface,<sup>44,45</sup> being a proposal for the bands positioning for Ta<sub>2</sub>O<sub>5</sub>/BiVO<sub>4</sub> heterojunction.

A similar case of n-n heterojunction (ZnWO<sub>4</sub>/CdS) was reported by Xu *et al.*,<sup>44</sup> where after the excitation of the semiconductors, an electric field is formed that facilitates the flow of electrons from the CdS towards the ZnWO<sub>4</sub>, which has an energetically unfavorable individual conduction band for the charge transfer. Similarly, the Ta<sub>2</sub>O<sub>5</sub>/BiVO<sub>4</sub> heterojunction presents a higher Ta<sub>2</sub>O<sub>5</sub> conduction band, not allowing electron transfer from BiVO<sub>4</sub> to Ta<sub>2</sub>O<sub>5</sub>. Under irradiation both BiVO<sub>4</sub> and Ta<sub>2</sub>O<sub>5</sub> components are excited. When physical mixing occurs (Ta<sub>2</sub>O<sub>5</sub>/BiVO<sub>4</sub>-M), the absence of the interface between the semiconductors makes them act individually in the photocatalysis process (Figure 9b). The electrons photogenerated by Ta<sub>2</sub>O<sub>5</sub> are applied in the H<sub>2</sub> production, while recombination of photogenerated charge carriers in BiVO<sub>4</sub> occurs due to the unfavorable energy level for the H<sub>2</sub> production.<sup>46</sup> In the n-n heterojunction formed through hydrothermal treatment (Ta<sub>2</sub>O<sub>5</sub>/BiVO<sub>4</sub>-H, Figure 9c), the excitation of the system produces charge carriers in both semiconductors. It is suggested that, as observed by Xu *et al.*,<sup>44</sup> the electric field formed after semiconductor excitation allows a flow of electrons to the interface region, allowing the improvement of the heterojunction performance in the hydrogen production due to the better

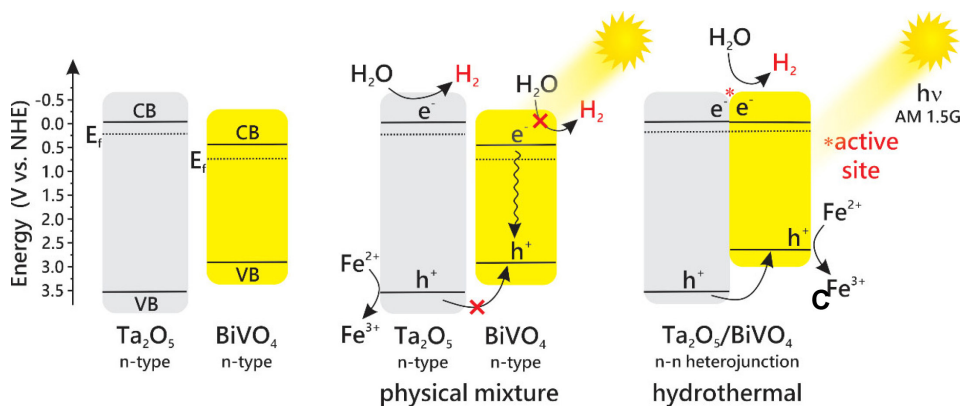


**Figure 9.** (a) Relative energy levels of the bands of Ta<sub>2</sub>O<sub>5</sub> and BiVO<sub>4</sub> semiconductors before the heterojunction formation. The possible photocatalytic mechanism for H<sub>2</sub> evolution with Ta<sub>2</sub>O<sub>5</sub>/BiVO<sub>4</sub> under simulated sunlight irradiation in the sample produced through the (b) physical mixture and by (c) hydrothermal treatment.

optical absorption of BiVO<sub>4</sub> in the visible region. As the composite is in contact with a sacrificial agent, while the Fe<sup>2+</sup> species consume the photoholes formed at the VB of BiVO<sub>4</sub>, minority carriers (holes) are transferred from the VB of Ta<sub>2</sub>O<sub>5</sub> to the VB of BiVO<sub>4</sub> through the optimized heterostructure, inhibiting the electron-hole recombination in the structure of Ta<sub>2</sub>O<sub>5</sub>. This justifies the low efficiency of the mechanical mixture (Ta<sub>2</sub>O<sub>5</sub>/BiVO<sub>4</sub>-M) for photocatalysis and the improvement shown by the material after hydrothermal treatment. Thus, the hydrothermally-treated Ta<sub>2</sub>O<sub>5</sub>/BiVO<sub>4</sub> presents a great increase in the interface between the semiconductors in addition to enabling the n-n heterojunction produced to be promising in the treatment of environmental effluents and the production of clean energy, contributing to green chemistry and materials engineering.

## Conclusions

In summary, the n-n type heterojunction formed by Ta<sub>2</sub>O<sub>5</sub>/BiVO<sub>4</sub> was prepared for the first time and its optical, structural, and photocatalytic properties were successfully investigated. Hydrothermal treatment improves the interface between semiconductors and promotes electronic transport between them, increasing the photocatalytic performance for hydrogen production. The heterojunction formation improves the adsorptive capacity of BiVO<sub>4</sub>, improving the photocatalytic performance of the material for MB degradation. The Ta<sub>2</sub>O<sub>5</sub>/BiVO<sub>4</sub> heterojunction presents improved performance for H<sub>2</sub> production, being 1.49 times higher than that of pure Ta<sub>2</sub>O<sub>5</sub> nanotubes. The n-n Ta<sub>2</sub>O<sub>5</sub>/BiVO<sub>4</sub> heterojunction is a promising material for the photocatalytic conversion of sunlight to produce clean energy through hydrogen and for environmental remediation, as in the photodegradation of the MB dye.

## Supplementary Information

Supplementary information (band structure estimation, supplementary figures, and supplementary tables) is available free of charge at <http://jbc.sqb.org.br> as PDF file.

## Acknowledgments

H. B. Gonçalves (IBPG-0740-3.03/16) is grateful for the scholarship of FACEPE. D. V. Freitas (302167/2021-8) acknowledges for a scholarship provided by CNPq. The authors also thank the staff at the Centro de Tecnologias Estratégicas do Nordeste (CETENE) for the characterization facilities. This work was supported by the following Brazilian research agencies: CNPq (442477/2019-8,

308504-2017-8, 424116/2018-9), FACEPE (APQ-515-9.25/19), CAPES, FUNASA and FINEP.

## Author Contributions

Henrique B. Gonçalves was responsible for conceptualization, data curation, formal analysis, investigation, writing original draft; Denilson V. Freitas for formal analysis, visualization, writing original draft, writing-review and editing; Emanuely J. Souza for formal analysis, validation; Maurício A. Melo for visualization, writing-review and editing; Johan Rene González-Moya for investigation, methodology, supervision, visualization; Eduardo Padrón-Hernández for supervision, visualization; Sherdil Khan for supervision, visualization, writing-review and editing; Giovanna Machado for conceptualization, funding acquisition, project administration, investigation, resources, supervision, writing-review and editing.

## References

1. Yang, L.; Hong, Y.; Liu, E.; Zhang, X.; Wang, L.; Lin, X.; Shi, J.; *Sep. Purif. Technol.* **2021**, *263*, 118366.
2. Takata, T.; Pan, C.; Domen, K.; *Sci. Technol. Adv. Mater.* **2015**, *16*, 033506.
3. Ali, S.; Li, Z.; Chen, S.; Zada, A.; Khan, I.; Khan, I.; Ali, W.; Shaheen, S.; Qu, Y.; Jing, L.; *Catal. Today* **2019**, *335*, 557.
4. Ahmed, M.; Xinxin, G.; *Inorg. Chem. Front.* **2016**, *3*, 578.
5. Chachvalvutikul, A.; Luangwanta, T.; Pattison, S.; Hutchings, G. J.; Kaowphong, S.; *Appl. Surf. Sci.* **2021**, *544*, 148885.
6. Ullah, H.; Rahman, A. U.; Aragão, E. L.; Barbosa, F. F. A.; Pergher, K. G. R.; Giulian, R.; Júnior, H. C.; Sommer, R. L.; Khan, S.; *Appl. Surf. Sci.* **2021**, *556*, 149694.
7. Fernandes, J. A.; Migowski, P.; Fabrim, Z.; Feil, A. F.; Rosa, G.; Khan, S.; Machado, G. J.; Fichtner, P. F. P.; Teixeira, S. R.; Santos, M. J. L.; Dupont, J.; *Phys. Chem. Chem. Phys.* **2014**, *16*, 9148.
8. Zhang, P.; Zhang, J.; Gong, J.; *Chem. Soc. Rev.* **2014**, *43*, 4395.
9. Adhikari, S. P.; Hood, Z. D.; More, K. L.; Ivanov, I.; Zhang, L.; Gross, M.; Lachgar, A.; *RSC Adv.* **2015**, *5*, 54998.
10. Gonçalves, R. V.; Wender, H.; Migowski, P.; Feil, A. F.; Eberhardt, D.; Boita, J.; Khan, S.; Machado, G.; Dupont, J.; Teixeira, S. R.; *J. Phys. Chem. C* **2017**, *121*, 5855.
11. Hu, Y.; Fan, J.; Pu, C.; Li, H.; Liu, E.; Hu, X.; *J. Photochem. Photobiol., A* **2017**, *337*, 172.
12. Sun, S.; Wang, W.; *RSC Adv.* **2014**, *4*, 47136.
13. Nagabhushana, G. P.; Nagaraju, G.; Chandrappa, G. T.; *J. Mater. Chem. A* **2013**, *1*, 388.
14. Xue, D.; Wang, J.; Wang, Y.; Sun, G.; Cao, J.; Bala, H.; Zhang, Z.; *Nanomaterials* **2019**, *9*, 351.
15. He, X.; Gan, J.; Li, H.; *J. Taiwan Inst. Chem. Eng.* **2021**, *127*, 119.

16. Liu, K.; Zhang, H.; Muhammad, Y.; Fu, T.; Tang, R.; Tong, Z.; Wang, Y.; *Sep. Purif. Technol.* **2021**, *274*, 118992.
17. Ma, L.; Xu, J.; Li, L.; Mao, M.; Zhao, S.; *New J. Chem.* **2020**, *44*, 18326.
18. Carmona, R. J.; Velasco, L. F.; Hidalgo, M. C.; Navío, J. A.; Ania, C. O.; *Appl. Catal., A* **2015**, *505*, 467.
19. Melo, M. A.; Wu, Z.; Nail, B. A.; de Denko, A. T.; Nogueira, A. F.; Osterloh, F. E.; *Nano Lett.* **2018**, *18*, 805.
20. Gonçalves, R. V.; Migowski, P.; Wender, H.; Eberhardt, D.; Weibel, D. E.; Sonaglio, F. C.; Zapata, M. J. M.; Dupont, J.; Feil, A. F.; Teixeira, S. R.; *J. Phys. Chem. C* **2012**, *116*, 14022.
21. Kato, H.; Kudo, A.; *Chem. Phys. Lett.* **1998**, *295*, 487.
22. Khan, S.; Zapata, M. J. M.; Baptista, D. L.; Gonçalves, R. V.; Fernandes, J. A.; Dupont, J.; Santos, M. J. L.; Teixeira, S. R.; *J. Phys. Chem. C* **2015**, *119*, 19906.
23. Khan, S.; Teixeira, S. R.; Santos, M. J. L.; *RSC Adv.* **2015**, *5*, 103284.
24. Stephenson, N. C.; Roth, R. S.; *Acta Crystallogr., Sect. B: Struct. Crystallogr. Cryst. Chem.* **1971**, *27*, 1037.
25. Hecht, H. G.; *J. Res. Natl. Bur. Stand., Sect. A* **1976**, *80A*, 567.
26. Suram, S. K.; Newhouse, P. F.; Gregoire, J. M.; *ACS Comb. Sci.* **2016**, *18*, 673.
27. Cooper, J. K.; Gul, S.; Toma, F. M.; Chen, L.; Liu, Y.-S.; Guo, J.; Ager, J. W.; Yano, J.; Sharp, I. D.; *J. Phys. Chem. C* **2015**, *119*, 2969.
28. Kukli, K.; Aarik, J.; Aidla, A.; Kohan, O.; Uustare, T.; Sammelselg, V.; *Thin Solid Films* **1995**, *260*, 135.
29. Qu, Z.; Liu, P.; Yang, X.; Wang, F.; Zhang, W.; Fei, C.; *Materials (Basel)* **2016**, *9*, 129.
30. Zhao, Z.; Li, X.; Zhao, Q.; *Rare Met.* **2010**, *29*, 115.
31. Zhang, A.; Zhang, J.; Cui, N.; Tie, X.; An, Y.; Li, L.; *J. Mol. Catal. A: Chem.* **2009**, *304*, 28.
32. Mohamed, H. E. A.; Afridi, S.; Khalil, A. T.; Zohra, T.; Alam, M. M.; Ikram, A.; Shinwari, Z. K.; Maaza, M.; *AMB Express* **2019**, *9*, 200.
33. Tokunaga, S.; Kato, H.; Kudo, A.; *Chem. Mater.* **2001**, *13*, 4624.
34. Jo, W. J.; Kang, H. J.; Kong, K.-J.; Lee, Y. S.; Park, H.; Lee, Y.; Buonassisi, T.; Gleason, K. K.; Lee, J. S.; *Proc. Natl. Acad. Sci. U.S.A.* **2015**, *112*, 13774.
35. Malathi, A.; Madhavan, J.; Ashokkumar, M.; Arunachalam, P.; *Appl. Catal., A* **2018**, *555*, 47.
36. Roy, J. S.; Morency, S.; Messaddeq, Y.; *J. Photochem. Photobiol.* **2021**, *7*, 100037.
37. Sleight, A. W.; Chen, H.-Y.; Ferretti, A.; Cox, D. E.; *Mater. Res. Bull.* **1979**, *14*, 1571.
38. Joseph, C.; Bourson, P.; Fontana, M. D.; *J. Raman Spectrosc.* **2012**, *43*, 1146.
39. Dabal, P. S.; Katiyar, R. S.; Jiang, Y.; Guo, R.; Bhalla, A. S.; *J. Raman Spectrosc.* **2000**, *31*, 1061.
40. Han, R.; Melo, M. A.; Zhao, Z.; Wu, Z.; Osterloh, F. E.; *J. Phys. Chem. C* **2020**, *124*, 9724.
41. Li, F.; Kang, Y.; Chen, M.; Liu, G.; Lv, W.; Yao, K.; Chen, P.; Huang, H.; *Chemosphere* **2016**, *150*, 139.
42. Saxena, S.; Verma, A.; Asha, K.; Biswas, N. K.; Banerjee, A.; Satsangi, V. R.; Shrivastav, R.; Dass, S.; *Int. J. Hydrogen Energy* **2020**, *45*, 26746.
43. Soltani, T.; Tayyebi, A.; Lee, B.-K.; *Catal. Today* **2020**, *340*, 188.
44. Xu, M.; Ye, T.; Dai, F.; Yang, J.; Shen, J.; He, Q.; Chen, W.; Liang, N.; Zai, J.; Qian, X.; *ChemSusChem* **2015**, *8*, 1218.
45. Nogueira, A. C.; Gomes, L. E.; Ferencz, J. A. P.; Rodrigues, J. E. F. S.; Gonçalves, R. V.; Wender, H.; *J. Phys. Chem. C* **2019**, *123*, 25680.
46. Lu, Q.; Yu, Y.; Ma, Q.; Chen, B.; Zhang, H.; *Adv. Mater.* **2016**, *28*, 1917.

Submitted: September 30, 2021

Published online: January 5, 2022

